Abnormal high stability halide perovskite thin films and solar cells to alpha and gamma irradiations with varying fluence

Juvet N. Fru *, M. Diale,
Department of Physics, University of Pretoria, Private Bag X20, Hatfield 0028, South Africa

*Corresponding author. juvet.fru@tuks.co.za; juvetfru@gmail.com

Abstract

Solar cells (SCs) and thin films made of methylammonium lead tri-iodide ($MAPbI_3$) have demonstrated remarkable robustness when irradiated with alpha (He^{2+}) and gamma radiations from americium-241. This study investigates changes in the structure, absorption, and surface morphology of perovskite thin films, as well as the photoelectronic properties of $MAPbI_3$ SCs, with and without irradiation with He^{2+}. According to the XRD analysis, tetragonal $MAPbI_3$ showed increased crystallinity and a decrease in compression micro-strain with an increased flux of He^{2+}. UV–Vis absorption remained unchanged until the flux exceeded 7.36 x 10^{12} He^{2+} cm^{-2}. The bandgaps for irradiated films decreased similarly to pristine films up to a dose of 3.07 x 10^{12} $He^{2+}cm^{-2}$, with significant differences observed beyond this point. Digital images showed significant changes in thin films irradiated at fluences exceeding 3.07 x 10^{12} He^{2+} cm^{-2}, with pits forming in grains responsible for the changes, confirmed by scanning electron microscopy. In conclusion, this study found that $MAPbI_3$ thin films and SCs can withstand doses of He^{2+} up to 3.07 x 10^{12} He^{2+} cm^{-2} in a He^{2+} radiation environment.

Introduction

Due to the increasing number of space missions, including space tourism, the number of satellites and spacecraft in orbit is also increasing. Solar cells (SCs) are relied upon to continuously power these satellites and spacecraft. However, due to the harsh space environment, including exposure to strong radiation such as cosmic rays and ionizing radiation (such as protons, electrons, and alpha particles (He^{2+})), electronic devices and SCs are affected by defects that reduce their performance. Thus, strict specifications are necessary for space-based SCs, including high tolerance to radiation damage (Li et al., 2021), high reliability (Brandhorst et al., 2008), high specific power (Kim et al., 2021), low folding volume (King et al., 2006), low cost, and ease of fabrication.

For instance, a spacecraft in low Earth orbit is exposed to electrons at a rate of 1 MeV per second, (6.3 x 10^3 cm^{-2} s^{-1}) and protons at a rate of 1 x 10^4 cm^{-2} s^{-1} (Miyazawa et al., 2018). To meet these specifications, SCs based on gallium arsenide (GaAs) single junctions are often used instead of silicon SCs in space applications. This is due to their better radiation resistance and higher cell efficiency. However, GaAs-SCs are more difficult and expensive to manufacture because of the cost of equipment and material preparation.

Copper indium gallium selenide (CIGS) thin-film SCs have been identified as more cost-effective candidates for space applications than GaAs due to their very high resistance to space radiation. This is because of the self-healing mechanism caused by the mobility of copper, which promotes defect relaxation (Schock and Noufi, 2000). A self-healing material can return to its original state of health without external intervention. Despite their high radiation

tolerance, the disadvantages of CIGS thin-film SCs include low efficiency and high complexity, and the rarity of indium on the earth (Ramanujam and Singh, 2017).

Researchers have studied the hardness and resistance of halide perovskites (HP) and perovskite solar cells (PSC) to ionizing radiation with protons, electrons, neutrons, and gamma rays (Lang et al., 2016; Xu et al., 2021; Brus et al., 2017; Kim et al., 2019). They found that PSC and HP have a high tolerance to radiation damage and excellent stopping power, making them ideal for ionizing radiation applications (Tan et al., 2021; Nassan et al., 2015, 2016). PSCs have been shown to have a higher tolerance to protons, electrons, neutrons, and gamma radiations than GaAs and CIGS-SCs and can replace GaAs, crystalline silicon, and CIGS SCs in electronic devices operating in space and radiation environments because they are easy to fabricate, have low cost and high efficiency.

Lang et al. compared the tolerance of PSC to proton irradiation with that of crystalline silicon SC (Lang et al., 2016). The researchers demonstrated that PSCs can withstand a proton fluence of 64 MeV up to 10^{12} p^+ cm^{-2}, which is three times that of crystalline silicon (c-Si) SCs. When the proton dose exceeded 10^{13} p^+ cm^{-2}, power conversion efficiency (PCE) and short-circuit current (J_{sc}) decreased, but the fill factor (FF) and open-circuit voltage (V_{oc}) remained constant. The degradation of the SC performance could be attributed to proton-induced defects. This is because the irradiation of HPs with protons leads to significant ionization of their lattice structures, which eventually leads to the dissociation of their ionic and covalent bonds (Lang et al., 2016). However, after the termination of proton irradiation, self-healing of perovskite took place, resulting in the recovery of J_{sc} and an increase in FF and V_{oc}. They explained self-healing by the fact that the displaced hydrogen atoms migrate within the perovskite lattice and passivate both pre-existing defects and proton-induced defects. Self-healing in HPs is also explained by the ease of ion migration, which allows displaced ions to retake their thermodynamically less energetic lattice sites (Yang et al., 2019).

According to Brus et al., their PSC could withstand 68-MeV proton irradiation (fluence rate 1.68 x10^9 p + cm^{-2} s^{-1}) with doses up to 10^{13} p^+ cm^{-2} (Brus et al., 2017). Another batch of PSC could withstand doses of up to 10^{13} p^+ cm^{-2} when exposed to 50 keV proton irradiation at an incident rate of 3×10^{11} $cm^{-2}s^{-1}$ (Miyazawa et al., 2018). Regarding the hardness of HPs to irradiated electrons, Miyazawa et al. compared the tolerance of P3HT-PSC after irradiation with a fluence of 1 x 10^{16} electrons cm^{-2} with the tolerance of crystalline silicon (c-Si) and triple-junction compound semiconductors of group's III-IV elements (Miyazawa et al., 2018). Based on their results, they found that the PSCs were least damaged by electron beams and had sufficiently high durability compared to c-Si and III-V composite SCs.

Under a 1.0 x 10^{15} cm^{-2} electron beam, there was an insignificant change in FF and PCE but a significant change in short-circuit current (Song et al., 2020). The loss of short-circuit current was mainly explained by the decreasing transmittance of the fluorine-doped tin oxide (FTO) substrate and partly by the degradation of the active perovskite layer. In a study conducted by Yang et al., it was demonstrated that HP is highly resistant to both gamma and visible radiation after 1535 h of exposure to a cumulative dose of 2.3 Mrad of gamma radiation (Yang et al., 2019). When tested for long-term radiation stability, Yang et al. found that 96.8% of the original PCE of PSC was retained after correction for light intensity. The radiation damage tolerance of PSC is generally due to the self-healing (self-repair) mechanism of HP, which is caused by ion migration (Lang et al., 2016; Xu et al., 2021).

Galactic cosmic radiations from outside our solar system consist of 85% protons and 14% He^{2+} (Nwankwo et al., 2020). Moreover, the carrier removal rate of the incident ionizing radiations, which determines the lifetime of electronics in radiation environments, is highest for He^{2+} irradiation (Kim et al., 2019). This implies that damages due to He^{2+} irradiation cannot be underestimated in outer space environments. Although galactic cosmic radiations contain significant amounts of alpha particles, halide PSCs have not been tested for He^{2+} tolerance.

We present the first study on the effects of He^{2+} irradiation on $MAPbI_3$ thin films and ITO/mesoporous-TiO_2/compact-TiO_2/$MAPbI_3$/Au solar cells (SCs). We prepared $MAPbI_3$ irradiated and pristine samples using sequential vacuum deposition (SVD) of single layers of PbI_2 and MAI. Then, we exposed the irradiated sample to He^{2+} (5.5 MeV) and gamma rays (59.5 keV) emitted by Am-214 radioactive isotopes (He et al., 2019) at ambient conditions. In contrast, we kept the pristine sample in the ambient environment without exposing it to radiation. We measured the X-ray diffractograms, optical absorption spectra, and surface micrographs of the irradiated and pristine samples after specific time intervals. The radiation dose was computed by multiplying the fluence ($7.1x10^6$ cm^{-2} s^{-1}) by the time (s). We also monitored the irradiated and pristine ITO/mesoporous-TiO_2/compact-TiO_2/$MAPbI_3$/Au SCs over time to understand changes in FF, V_{oc}, and PCE. Our investigation aimed to determine the radiation hardness of $MAPbI_3$ SCs under 5.5 MeV He^{2+} and 59.5 keV gamma radiation.

The energy of gamma rays, which is 59.5 keV, is much lower than that of alpha particles, which is 5.5 MeV. Additionally, alpha particles are more ionizing than gamma rays and are expected to cause significantly more ionization and damage than gamma rays. Therefore, the effect of gamma rays can be neglected when using this source.

2. Experimental

2.1. SVD of $MAPbI_3$

Fig. 1 illustrates the process of growing 3D $MAPbI_3$ perovskites through SVD, a technique that Fru and colleagues have already optimized (Fru et al., 2020a). The evaporation chamber was mounted with FTO substrates to be used for the film preparation. The deposition chamber contained lead (II) iodide (PbI_2) and methylammonium iodide (MAI) in boron nitride crucibles. An apropriate vacuum level of 2.0 x 10^{-5} mbars was achieved by pumping air out of the chamber. Initially, a suitable current was applied to the coils surrounding the crucible to evaporate 100 nm of PbI_2. Subsequently, 400 nm of MAI was evaporated. The thickness of thin films was measured using a quartz crystal monitor built into the deposition apparatus. The thickness of PbI_2 was measured using a density of 6.16 g cm^{-3} and a Z-factor of 1.10, while the thickness of MAI was measured using a density of 1.20 g cm^{-3} and a Z-factor of 2.70 (Fru et al., 2021; Mayimele et al., 2022). In contrast to other evaporation processes where a separate heat source is used to heat the substrate during deposition (Abdallah et al., 2021), in this study, the heat from the chamber during the evaporation process was the only source of substrate heating. After extraction from the chamber, the sample was annealed in air at 100 ◦C for 10 min.

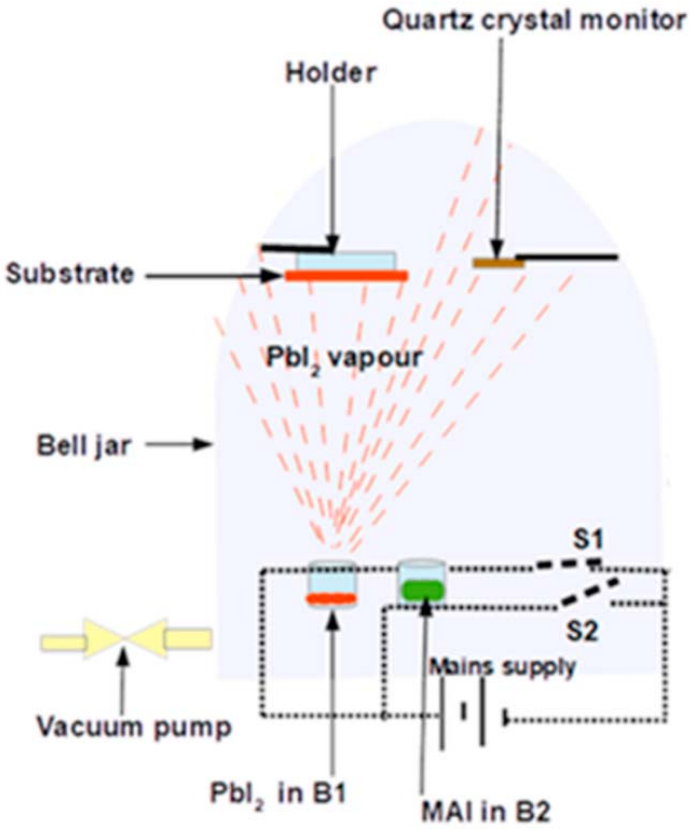

Fig. 1. Simplified diagram for deposition of $MAPbI_3$ by SVD.

A Bruker D2-Phaser X-ray diffractometer using Cu Kα radiation with a wavelength of 1.5405 Å was used to determine the diffractograms of the thin films. The two 2 Θ angles between the incident and diffracted X-ray beams were varied from 20 to 60◦ at a scanning rate of $0.05^{\circ}s^{-1}$. The morphological properties were observed using a field emission scanning electron microscope (FE-SEM Zeiss Crossbeam 540) with an accelerating voltage of 2.0 kV. The average grain sizes were determined from the FE-SEM images using ImageJ software. The optical absorption spectra of the films were measured using an Agilent CARY 60 UV–Vis spectrometer, with incident light wavelengths ranging from 400 to 800 nm.

2.2. Williamson-Hall (W–H) method and Tauc plots

2.2.1. Williamson-Hall (W–H) method

Williamson-Hall (W–H) method was used to calculate crystallite size and microstrain from XRD patterns (Williamson and Hall, 1953), as explained in previous studies (Fru et al., 2020a, 2020b). To this end, the full-width half maximum (FWHM) of each peak in the diffractograms was first determined using a Gaussian fit and then used for W–H analysis according to Equation (1),

$$FWHM\cos\theta = \frac{K\lambda}{D} + 4\varepsilon\sin\theta \qquad \text{Equation 1}$$

where K is the Scherrer constant (0.94 for spherical crystallites with cubic symmetry), θ is Bragg's diffraction angle, ε is the microstrain, λ is the wavelength and D is the average crystallite size. A graph of FWHM cos θ against 4 sin θ was plotted and its slope and intercept are determined and used to calculate D and ε.

2.2.2. Tauc plot

Tauc drafted a method to calculate the bandgap of amorphous semiconductors using optical absorption spectra (Redinger and Siebentritt, 2015). Mott and Davis developed the Tauc approach further (Mott and Davis, 1970). The Mott and Davis equation (Equation (2)) is used to plot the Tauc graphs,

$$(\alpha h\upsilon)^{\frac{1}{n}} = A\left(h\upsilon - E_g\right) \qquad \text{Equation 2}$$

In Equation (2), E_g is a bandgap while A is a proportionality constant, α is the absorption coefficient, h is the Planck constant, υ is the frequency, and n is a numerical constant that determines the nature of the transition; n equals 1/2, 2, 3/2, and 3 for directly allowed transfers, indirectly transferred transfers, directly forbidden transfers, and indirectly forbidden transfers, respectively.

2.3. Solar cell fabrication

ITO Glass substrates (S211, Ossila) were used to fabricate two SCs with dimensions of 20 x 15 mm. In acetone, ethanol, and DI water, the substrates were sequentially sonicated for 10 min and dried with pressurized nitrogen flow. During the deposition of an electron transport layer (ETL) of titanium dioxide compact (c-TiO_2), a heat-resistant tape was applied to the ends of the cleaned, patterned substrates. To prepare the precursor solution for the c-TiO_2 layer, 0.55 ml of titanium diisopropoxide bis (acetylacetonate) was mixed with 5 ml of 1-butanol to yield 0.3 M TiO_x. C–TiO_2 was deposited by spinning the 0.3 M TiOx solution at 3000 rpm for 30 s on the ITO substrate. The deposited film was dried in a 125 ◦C oven for 5 min. After the experiment is repeated once, the heat-resistant tape is removed and the sample is annealed in a

furnace for 30 min at 500 ◦C. After covering the ends once more with heat-resistant tape, a mesoporous titanium dioxide (m-TiO_2) layer was prepared on top of the c-TiO2. To prepare the paste for deposition of m-TiO_2, 1.2 g of TiO_2 nanoparticles were dissolved in 10 ml of ethanol, 4 ml of terpineol, and 10% ethyl cellulose (0.6 g of ethyl cellulose in 10 ml of ethanol). After being stirred at room temperature overnight, the mixture was filtered. The paste was spin-cast at 3000 rpm for 30 s, followed by 5 min of drying at 125 ◦C. To form the mesoporous-TiO_2 (m-T TiO_2) layer, the heat-resistant tape was removed, and annealing at 500 ◦C for 30 min was performed. Both ends of the device were covered and the $MAPbI_3$ active layer was prepared as described above. The tape was removed and the covered section was cleaned using cotton earbuds soaked in epoxy resin (Ossila). A heat-resistant tape is used to protect the contacts from being covered with c- TiO_2 and m- TiO_2 during spin coating, and also because the c- TiO_2 layer is dried at 125 ◦C before deposition of m- TiO_2. Eight individual pixels of gold contacts were deposited using the cathode deposition mask (E501) from Ossila. One of the SC was irradiated with He^{2+} from Am-241 while exposed to ambient conditions, as shown in Fig. 2(a). The irradiation was carried out by mounting the source on the rear of the solar cell, allowing direct contact between the radiation and the halide perovskite material whose hardness was tested. The irradiation source was removed at specific time intervals before

measuring the efficiency of SC. The PCE of the unirradiated (pristine) SC shown in Fig. 2(b) was measured for the same time intervals.

SCs were measured using an automatic I–V measurement system (Ossila) to determine their current density-voltage characteristics and device performance parameters under illumination. Solar simulator irradiated measurements are conducted using an Oriel LCS-100TM Small Area So11A Series by Newport. The conditions for the simulated solar output were set at 100 mW/cm2 with reference spectral filtering of AM1.5 G.

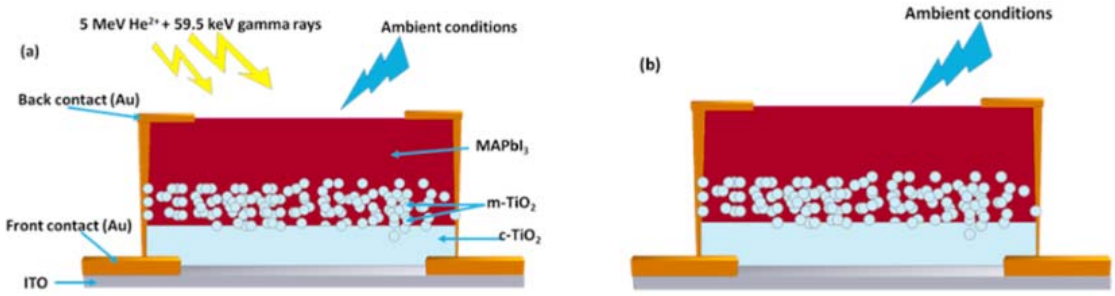

Fig. 2. (a) Irradiated $MAPbI_3$-based SC, and (b) pristine $MAPbI_3$-based SC.

3. Discussion of results

3.1. Structural properties

Fig. 3 presents the XRD patterns of $MAPbI_3$ films, both pristine and irradiated, for various time intervals. The pristine films were exposed only to ambient conditions, while the irradiated films were exposed to both ambient conditions and He^{2+}. For the irradiated samples, the time intervals were converted to He^{2+} fluence by multiplying the time intervals with the fluence rate ($7.1x10^6$ cm^{-2} s^{-1}). The diffractograms confirmed the tetragonal crystal structure of $MAPbI_3$ with the I4/mcm space group, as observed in previous studies (Fru et al., 2020a; Shi et al., 2015; Saidaminov et al., 2015; Jeon et al., 2014). Additional peaks at 26.7, 33.9, and 37.9◦ were matched to FTO using JCPDS card number 00-005-0467. The as-deposited images showed the presence of the (001) plane of PbI_2 on the pristine sample, but not on the irradiated sample. These films were simultaneously deposited under the same conditions, with the only difference being the position of the substrates on the holder, leading to the presence of a PbI_2 peak on the as-deposited pristine sample and the absence of PbI_2 on the as-deposited irradiated sample. This suggests that the complete formation of $MAPbI_3$ film could depend on the horizontal position of the substrate within the chamber. However, in this study, changes in irradiated and pristine thin films were followed independently, so this fact did not affect the results.

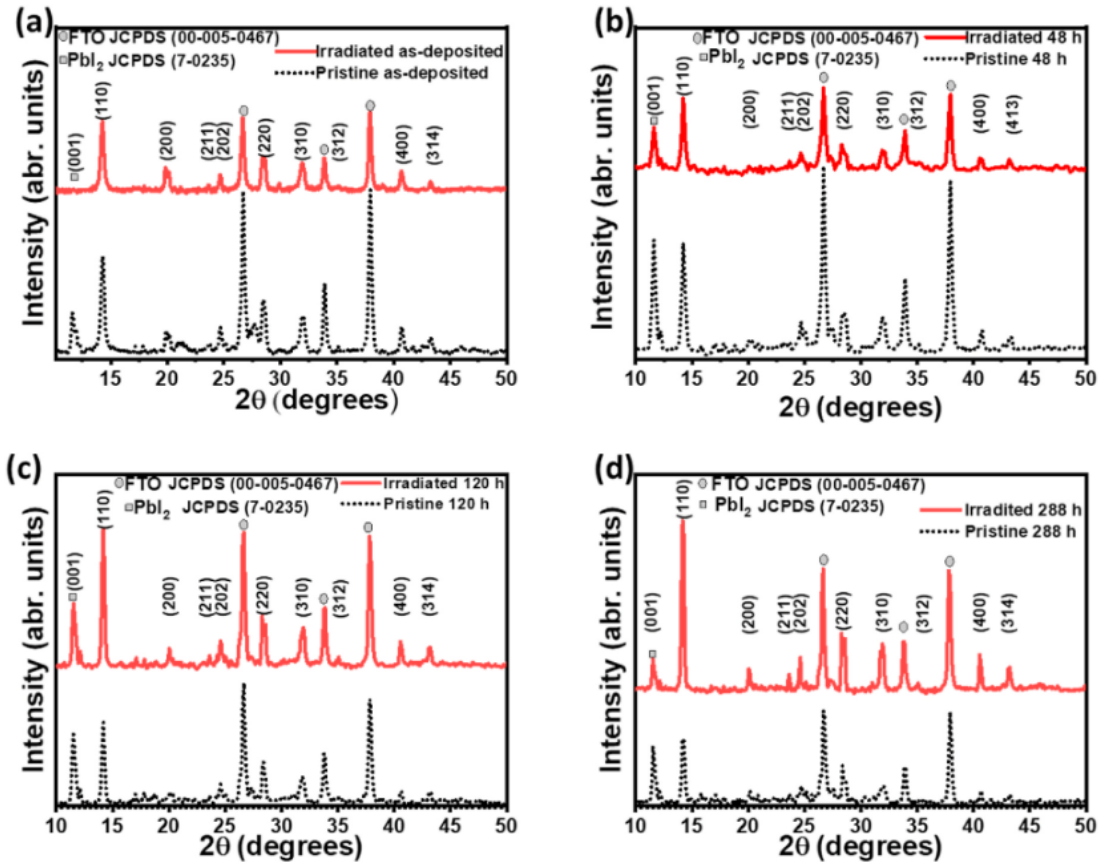

Fig. 3. Diffractograms of irradiated and pristine $MAPbI_3$ on FTO substrate at various times (a) as-deposited (b) 48 h after deposition (c) 120 h after irradiation and (d) 288 h after irradiation.

The prominent peak of PbI_2 at 11.6◦ was observed in both pristine and irradiated samples, indicating an unreacted precursor during the formation of $MAPbI_3$ by either a solution or a vapor process (Fru et al., 2020a; Shi et al., 2015; Saidaminov et al., 2015; Jeon et al., 2014; Alidaei et al., 2020). This peak was indexed with the JCPDS number 7–0235 (Shkir et al., 2019). The intensity of the PbI_2 peak increased with time for both pristine and irradiated samples. This increase in intensity could be due to the fragmentation of the large $MAPbI_3$ grains into nano-grains of PbI_2 when exposed to humid air (Alberti et al., 2019). The intensities of the prominent peaks of $MAPbI_3$ in the irradiated sample increased with fluence, indicating that an increase in alpha particle fluence on the irradiated film could lead to an increase in the crystallinity of $MAPbI_3$ thin films.

The average crystallite size and microstrain of irradiated and pristine $MAPbI_3$ thin films are presented in Fig. 4. Fig. 4(a) illustrates the change in average crystallite size over time for both irradiated and pristine samples. The results reveal that the average crystallite size of the irradiated sample continuously increased, indicating a persistent increase in crystallinity. On the other hand, the average crystallite size of the pristine sample increased up to 120 h and then decreased. It is suggested that the increase in diffractogram intensity might be due to the increase in layer thickness and crystallinity. However, irradiation is not likely to cause an increase in film thickness, and the increase in crystallinity could be attributed to an increase in the dose of He^{2+}. This observation aligns with the findings of other researchers who have

reported that ion irradiation enhances the crystallinity of thin films (Chiu et al., 2015; Ali et al., 2020; Oryema et al., 2022).

Fig. 4(b), the change in micro-strain with time is presented for both irradiated and pristine samples. The micro-strains are negative, indicating a compressive nature. This result is consistent with previous reports on $MAPbI_3$ thin films (Kim and Park, 2020). Furthermore, the micro-strain in both samples gradually relaxes over time, which could lead to a decrease in defect density and an increase in charge carrier lifetime (Kim and Park, 2020).

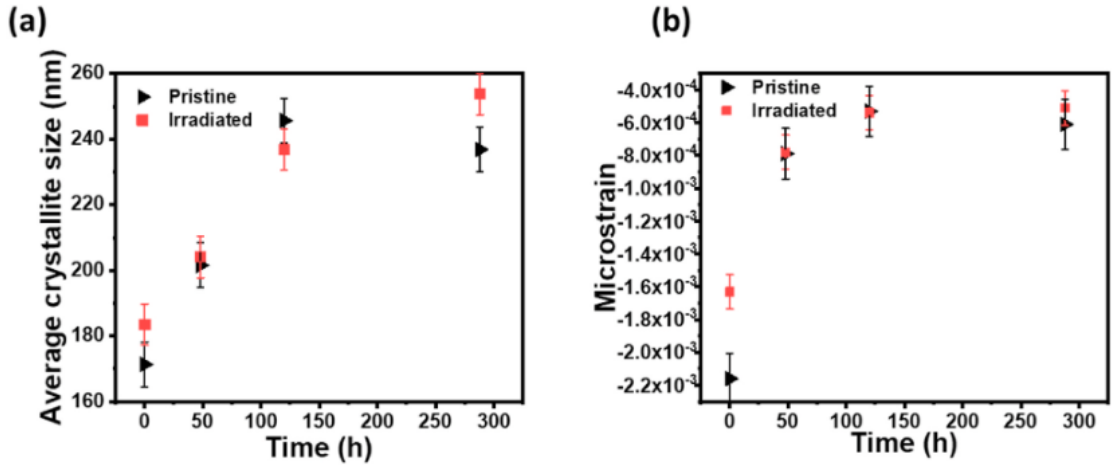

Fig. 4. Average crystallite size and micro-strain of irradiated and pristine $MAPbI_3$ thin films at various times. (a) Average crystallite size vs. time (error bars showing the standard deviation of the average grain size distribution, scaling factor 0.2). (b) Micro-strain vs. time (error bars showing the standard deviation of the microstrain, scaling factor 0.2).

3.2. The properties of morphology

Fig. 5 presents digital images of irradiated and pristine samples at different time intervals. No significant changes in color were observed on the pristine sample, while yellowish spots appeared on the irradiated sample after 120 h, corresponding to a fluence of 3.07×10^{12} He^{2+} cm^{-2}. These color changes from the characteristic dark brownish color of $MAPbI_3$ to the yellowish color of PbI_2 may be linked to alpha particle-induced degradation of $MAPbI_3$ (Kundu and Kelly, 2020).

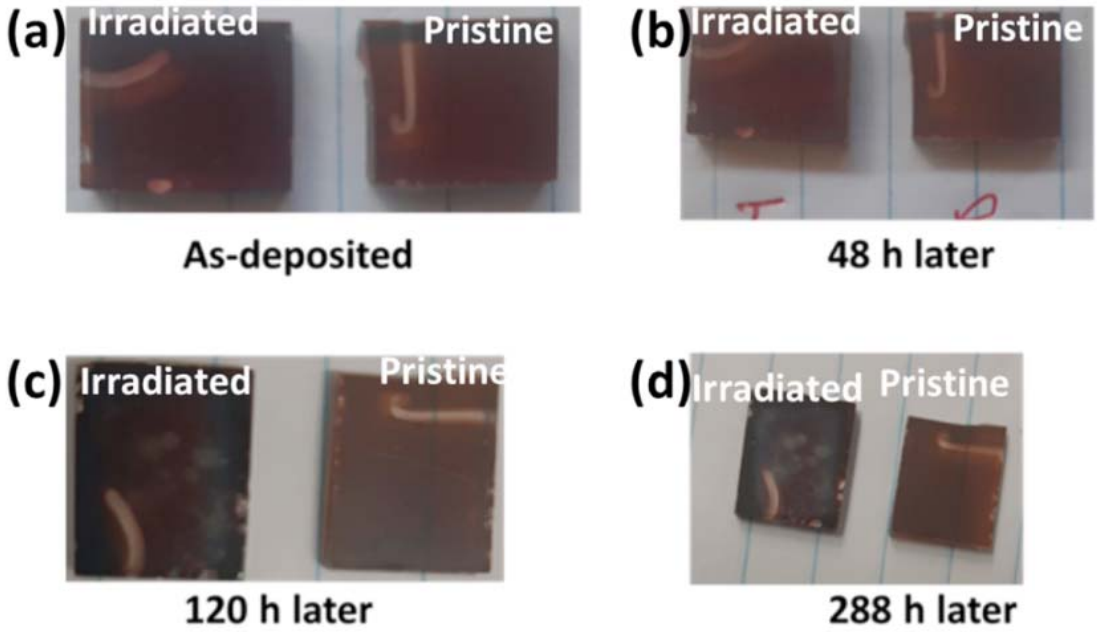

Fig. 5. Digital images of irradiated and pristine $MAPbI_3$ thin films after given time intervals, (a) as-deposited irradiated and pristine $MAPbI_3$ thin films, (b) irradiated and pristine $MAPbI_3$ thin films after 48 h, (c) irradiated and pristine $MAPbI_3$ thin films after120 h, and (d) irradiated and pristine $MAPbI_3$ thin films after 288 h.

Fig. 6 (a-d) shows SEM micrographs of the as-deposited irradiated and pristine samples after 288 h of deposition. The pristine samples showed an insignificant change in surface morphology, with only very few small white dots near grain boundaries after 288 h. This slight change in surface morphology indicates the stability of the sequential vacuum-deposited $MAPbI_3$ thin films in the air. Although the exact chemical composition of the white spots was not determined, based on previous reports, they could be attributed to PbI_2 (Chen et al., 2014). In contrast, pit holes were observed on the surface of the irradiated sample, as shown in Fig. 6 (d), which could be produced by the continuous bombardment of the grains by the He^{2+} during irradiation. In addition to the pit holes, the microscopic images of the sample irradiated after 288 h also showed white lines along the grain boundaries, as shown in Fig. 6 (d).

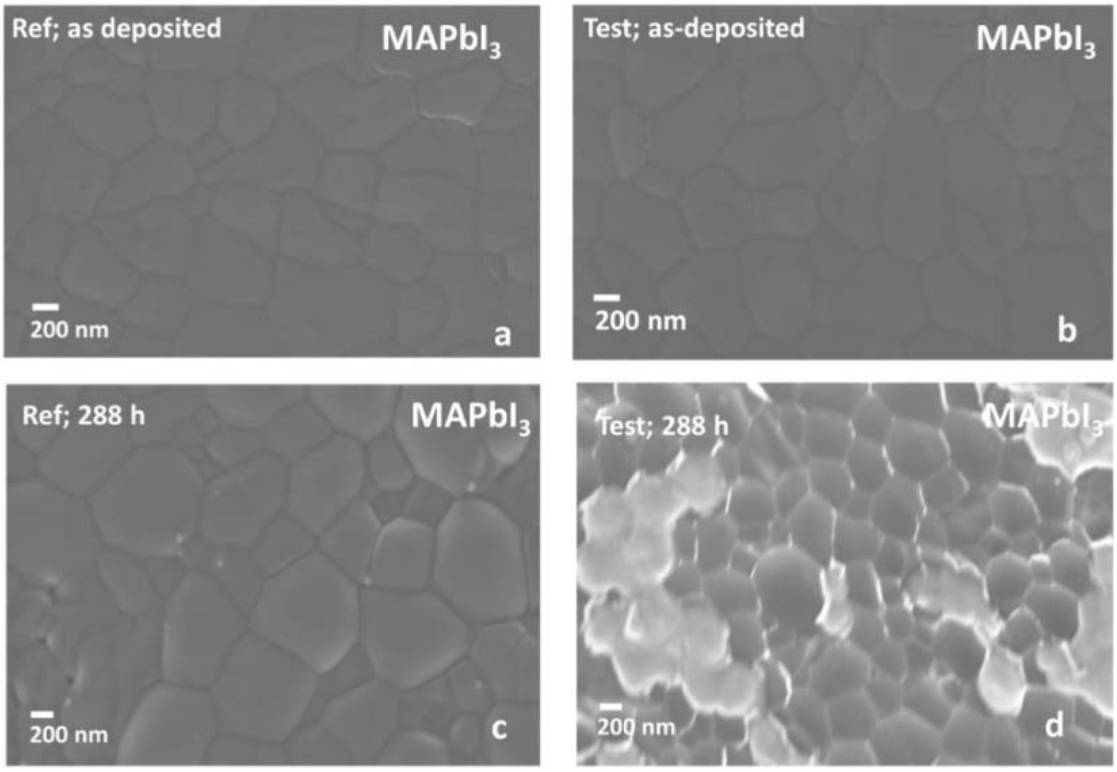

Fig. 6. FE-SEM micrographs of irradiated and pristine $MAPbI_3$ thin films, (a) as-deposited $MAPbI_3$ pristine sample, (b) as-deposited $MAPbI_3$ irradiated sample, (c) $MAPbI_3$ pristine sample after 288 h, and (d) $MAPbI_3$ irradiated sample 288 h under irradiation.

3.3. Optical properties

The effect of irradiation on the optical properties was investigated by monitoring the absorption spectra of the irradiated and pristine samples over time. Fig. 7 shows the absorption spectra of the pristine (Fig. 7(a)) and irradiated (Fig. 7(b)) $MAPbI_3$ thin films at various time intervals. A large reduction in absorption intensity was observed 48 h after deposition, after which the intensity remained almost constant for both samples. Thus, there was little change in absorbance of the irradiated sample up to a fluence of 7.36×10^{12} He^{2+} cm^{-2}, corresponding to 288 h of accumulated radiation. Irradiated thin films perform exceptionally well under He^{2+} irradiation, which proves how resistant they are. Additionally, Am-241 is a source of gamma rays as well as alpha particles (He et al., 2019), which means that $MAPbI_3$ has extraordinary resistance to both types of radiation. Boldyreva et al. previously demonstrated that $MAPbI_3$ is very stable under gamma rays (Boldyreva et al., 2020), and in 2019, they showed that the absorption spectra of tri-cation HP were not affected by gamma radiation (Boldyreva et al., 2019).

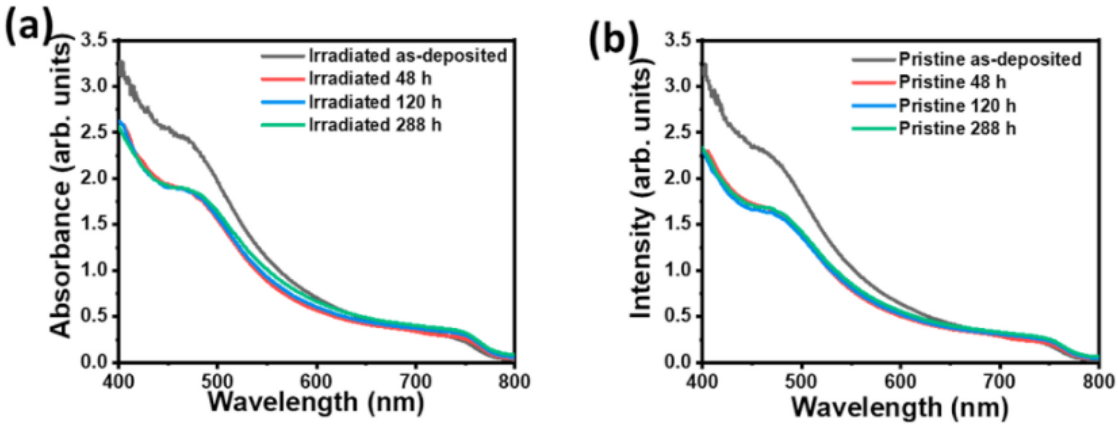

Fig. 7. The absorption spectrum of irradiated and pristine $MAPbI_3$ thin films, (a) absorption intensity vs. wavelength of the pristine sample at various time intervals, and (b) absorption intensity vs. wavelength of the irradiated sample at various time intervals.

The Tauc graphs used to calculate the bandgaps are presented in Fig. 8(a and b), while Fig. 8(c) shows the bandgap plotted against the time for both the irradiated and pristine $MAPbI_3$ thin films. The irradiated samples showed a similar reduction in bandgap compared to the pristine samples up to a fluence of 3.07×10^{12} He^{2+} cm^{-2}, beyond which the difference was substantial.

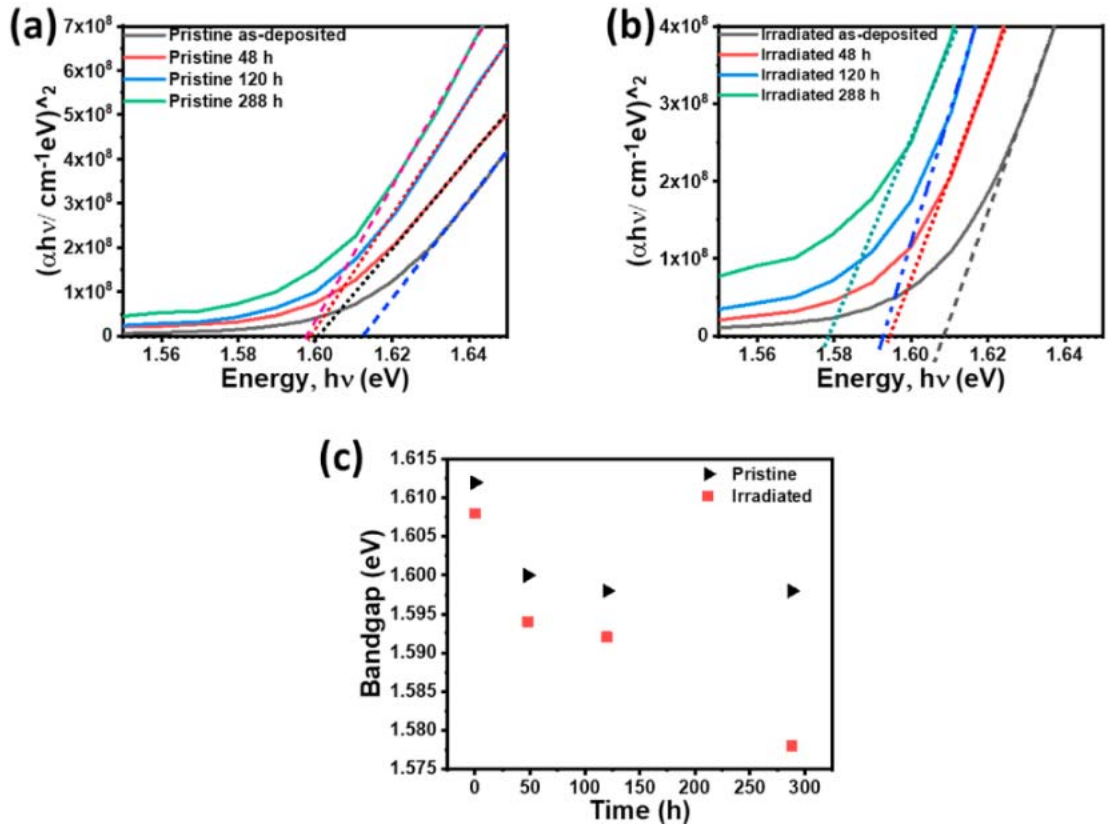

Fig. 8. (a) Tauc plot of $MAPbI_3$ pristine sample at various times, (b) Tauc plot of $MAPbI_3$ irradiated sample at various times, and (c) bandgap against a time of pristine and irradiated $MAPbI_3$ sample.

3.4. Electrical properties

Fig. 9 shows the J-V characteristics of the pristine (Fig. 9(a)) and irradiated (Fig. 9(b)) ITO/c-TiO_2/m-TiO_2/ $MAPbI_3$/Au SCs. As shown Fig. 10 (a), the PCE of both the irradiated and pristine SCs decreased over time, but the degradation of the irradiated SC was greater after 120h of irradiation. The FF decreased continuously for the irradiated sample, while the pristine sample showed an initial negative slope followed by a slightly positive slope, as shown in Fig. 10(b). The decrease in FF corresponds to that of a silicon solar cell after He^{2+} irradiation, which was previously associated with the formation of Frenkel defects that increase the resistance in the active layer (Siddiqui and Usman, 2021). The J_{sc} value decreased slowly in the pristine sample and rapidly in the irradiated sample, consistent with a decrease in the PCE value as shown in Fig. 10(c). In other words, the drop in J_{sc} is likely primarily responsible for the decrease in PCE. The deterioration of J_{sc} and V_{oc} could be due to a reduction in minority carrier lifespan due to recombination centers induced by He^{2+} radiation (Xu et al., 2018). The decrease in V_{oc} from its original value to the value 120 h later was more pronounced in the pristine sample than in the irradiated sample, as shown in Fig. 10(d).

Under ambient conditions, the pristine SC retains 93.1% of its original PCE after 120 h, whereas the irradiated SC retains 85.37% of its PCE for the same time, corresponding to a dose of 3.07×10^{12} He^{2+} cm^{-2}.

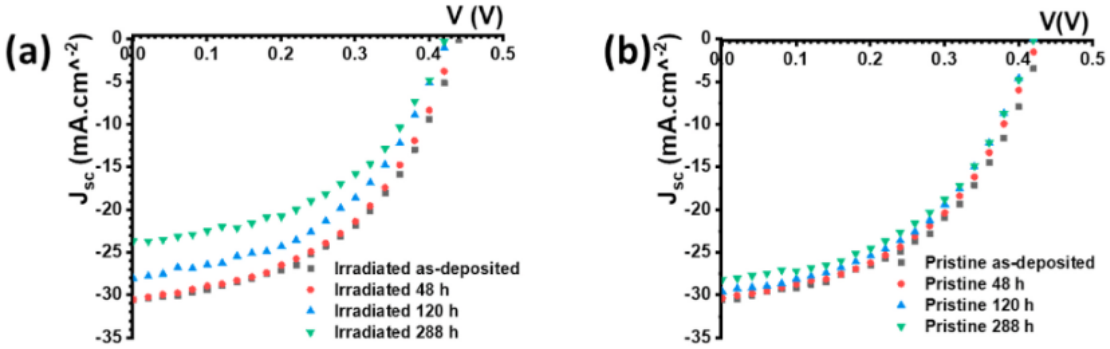

Fig. 9. (a) J-V characteristics of the pristine sample at various time intervals, and (b) J-V characteristics of the irradiated sample at various time intervals.

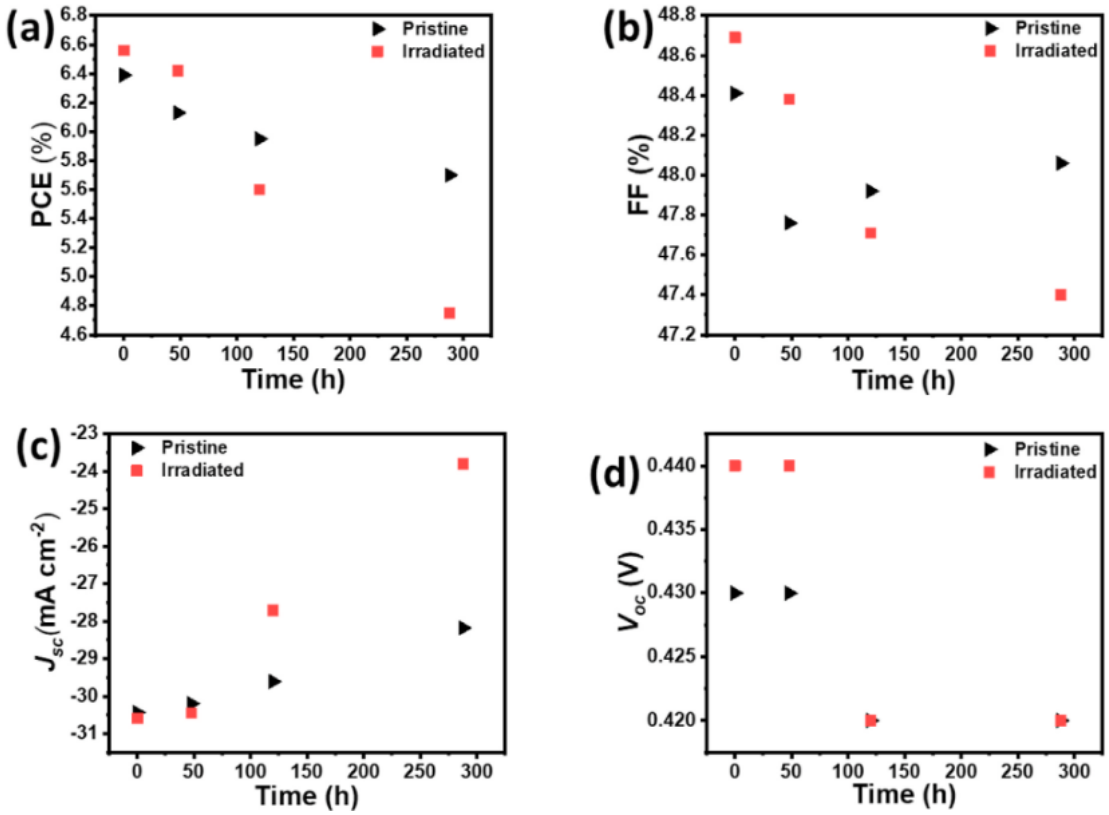

Fig. 10. PCE, FF, J_{sc}, and V_{oc} of pristine and irradiated samples at different time intervals, (a) PCE vs. time, (b) FF vs. time, (c) J_{sc} vs. time, and V_{oc} vs. time.

After 48 h of exposure to Am-241 (corresponding to a flux of 1.23 x 10^{12} He^{2+} cm^{-2}) plus ambient, the PCE and J_{sc} of the irradiated samples drop more rapidly than that of the pristine sample. Therefore, under normal atmospheric conditions, aging of the SCs leads to a reduction in PCE and J_{sc}, but the extent of degradation is greater for the irradiated samples.

If the effect of degradation due to ambient conditions were removed, then the irradiated SC would retain 92.3% of its initial PCE under an accumulated dose of 3.07 x 10^{12} He^{2+}+ cm^{-2}. This is calculated as follows: After 120 h in the air (ambient), corresponding to a dose of 3.07 x 10^{12} He^{2+} cm^{-2}, the irradiated SC retained 85.37% of its PCE, whereas the pristine SC under ambient-only conditions retained 93.1% of its original PCE for the same time. Thus, the effect of ambient is obtained by subtracting 93.1% from 100%, which gives 6.9%. Adding the effect (or correction due to environment) to the percentages of PCE retained by the irradiated sample yields 92.3%.

Mahapatra et al. also showed that the decrease in PCE with the aging time of $MAPbI_3$-based SCs was mainly due to a decrease in FF and J_{sc} (Mahapatra et al., 2020). It is important to note, however, that this performance degradation accelerates after the accumulation of a certain level of He^{2+} fluence within the irradiated sample. This is an extraordinary hardness to highly damaging He^{2+} radiations. In comparison, the highly radiation-resistant perovskite/CIGS tandem under 68 MeV proton irradiation could only retain 85% of its initial PCE at a dose of 2.0 x10^{12} p^{+} cm^{-2} (Lang et al., 2020).

Lang et al. (2019) discovered that the extraordinary hardness of triple cation perovskites was due to efficient de-trapping (prolonged release) of minority carriers from proton-irradiation-induced trap states (Lang et al., 2019). A surprising finding was that during PCE degradation of irradiated and pristine samples, neither FF nor V_{oc} was significantly affected, though small random variations were observed. An independent sample t-test was used to determine if there were significant differences between the mean values of FF and V_{oc} due to slight random variation. The P-values obtained were 0.9824 for FF and 0.4680 for V_{oc}. The P-values being greater than 0.05 are indicative that degradation and irradiation did not affect FF and V_{oc} at a significant level. One reason for this could be that the degradation is not due to the formation of traps (Boldyreva et al., 2019; Cowan et al., 2011). There is no doubt that traps and non-radiative loss channels increase the density of traps in the bandgap, leading to losses in V_{oc} (Cowan et al., 2011; Zhang et al., 2020). Besides, it has been shown that radiation-induced recombination centers in SCs largely contribute to the degradation of V_{oc} of InGaP/-GaAs/Ge SCs with an increase in 5.1 MeV alpha-particle absorbed dose (Xu et al., 2018).

Lang et al. showed that the change in FF and V_{oc} upon irradiating perovskite/CIGS tandem SC with 68 MeV proton irradiation at a dose of 2 x 10^{12} p+/cm2 was due to radiation-induced defects in the CIGS and not in the perovskite sub-SC (Lang et al., 2020). However, according to their previous work in 2016, there are proton-induced defects in $MAPbI_3$ SCs during irradiation, which are rapidly passivated by hydrogen after the irradiation source is removed (Lang et al., 2016). As a result, we propose that the self-healing in HP is quicker than in CIGS, and the fast self-healing mechanism in $MAPbI_3$ may explain its resistance to He^{2+} irradiation.

4. Conclusions

For the first time, we have demonstrated that $MAPbI_3$ thin films are highly resistant to 5.5 MeV He^{2+} and 59.5 keV gamma irradiations of 7.1x106 cm^{-2} s^{-1} fluence. The structural, optical, and morphological properties of $MAPbI_3$ thin films were not affected by He^{2+} irradiation up to an accumulated dose of 3.07 x 10^{12} He^{2+} cm^{-2}. Under ambient conditions, the pristine SC retained 93.1% of its initial PCE after 120 h. After 120 h in the air, the irradiated SC retained 85.37% of its PCE even after exposure to a dose of 3.07 x 10^{12} He^{2+} cm^{-2}. Thus, after the effect of degradation due to ambient conditions was removed, the irradiated $MAPbI_3$ SCs retained 92.3% of their initial PCE with an accumulated dose of 3.07 x 10^{12} He^{2+} cm^{-2}. The resistance of $MAPbI_3$ to 5.5 MeV He^{2+} and 59.5 keV gamma irradiations of 7.1x106 cm^{-2} s^{-1} fluence from AM-241 is similar to the hardness of triple cation perovskites ($Cs_{0.05}MA_{0.17}FA_{0.83}Pb(I_{0.83}Br_{0.17})_3$–64 MeV protons), which has previously been shown to be harder than CIGS. Based on our findings and earlier results on irradiations with protons and electrons, we conclude that PSCs have the potential to replace CIGS and other classic SCs used in space applications.

CRediT authorship contribution statement

Juvet N. Fru: Conceptualization, Data curation, Review & editing, Methodology, Writing of original draft, and **M. Diale:** Supervision, Project administration, Investigator-Funding acquisition.

Declaration of competing interest

All authors declare no conflict of interest.

Data availability

No data was used for the research described in the article.

Acknowledgments

For the financial support, the authors are deeply grateful to the University of Pretoria, the National Research Foundation, the NRF grant number N0115/115463 of SARChI, and the Externally Funded Post-Doctoral Fellowship Programme: Grant Cost Centre N0115/115463.

References

Abdallah, B., Kakhia, M., Obaide, A., 2021. Morphological and structural studies of ZnO nanotube films using thermal evaporation technique. Plasmonics 16, 1549–1556. https://doi.org/10.1007/s11468-021-01420-x.

Alberti, A., Bongiorno, C., Smecca, E., Deretzis, I., La Magna, A., Spinella, C., 2019. Pb clustering and PbI_2 nanofragmentation during methylammonium lead iodide perovskite degradation. Nat. Commun. 10, 2196. https://doi.org/10.1038/s41467-019-09909-0.

Ali, S.M., AlGarawi, M.S., Aldawood, S., Al Salman, S.A., AlGamdi, S.S., 2020. Influence of gamma irradiation on the properties of PbS thin films. Radiat. Phys. Chem. 171, 108732 https://doi.org/10.1016/j.radphyschem.2020.108732.

Alidaei, M., Izadifard, M., Ghazi, M.E., 2020. Improving the efficiency of perovskite solar cells using modification of CH3NH3PbI3 active layer: the effect of methylammonium iodide loading time. Opt. Quant. Electron. 52, 1–14. https://doi.org/10.1007/s11082-020-02327-3.

Boldyreva, A.G., Akbulatov, A.F., Tsarev, S.A., Luchkin, S.Y., Zhidkov, I.S., Kurmaev, E. Z., Stevenson, K.J., Petrov, V.G., Troshin, P.A., 2019. γ-Ray-induced degradation in the triple-cation perovskite solar cells. J. Phys. Chem. Lett. 10, 813–818. https://doi.org/10.1021/acs.jpclett.8b03222.

Boldyreva, A.G., Frolova, L.A., Zhidkov, I.S., Gutsev, L.G., Kurmaev, E.Z., Ramachandran, B.R., Petrov, V.G., Stevenson, K.J., Aldoshin, S.M., Troshin, P.A., 2020. Unravelling the material composition effects on the gamma ray stability of lead halide perovskite solar cells: $MAPbI_3$ breaks the records. J. Phys. Chem. Lett. 11, 2630–2636. https://doi.org/10.1021/acs.jpclett.0c00581.

Brandhorst, H., Rodiek, J., O'Neill, M., 2008. The Stretched Lens Array's Testing and Mission Success in Harsh Environments. Eur. Sp. Agency, (Special Publ. ESA SP. Brus, V.V., Lang, F., Bundesmann, J., Seidel, S., Denker, A., Rech, B., Landi, G., Neitzert, H.C., Rappich, J., Nickel, N.H., 2017. Defect dynamics in proton irradiated CH3NH3PbI3 perovskite solar cells. Adv. Electron. Mater. 3, 1600438 https://doi.org/10.1002/aelm.201600438.

Chen, Q., Zhou, H., Song, T., Luo, S., Hong, Z., Duan, H., Dou, L., Liu, Y., Yang, Y., 2014. Controllable self-induced passivation of hybrid lead iodide perovskites toward high performance solar cells. Nano Lett. 14, 4158–4163. https://doi.org/10.1021/nl501838y.

Chiu, P.-K., Chiang, D., Lee, C.-T., Lin, Y.-W., Hsiao, C.-N., 2015. Optical properties and crystallinity of silver mirrors under a 35 krad cobalt-60 radiation. J. Vac. Sci. Technol. A Vacuum, Surfaces, Film. 33, 05E104 https://doi.org/10.1116/1.4921525.

Cowan, S.R., Leong, W.L., Banerji, N., Dennler, G., Heeger, A.J., 2011. Identifying a threshold impurity level for organic solar cells: enhanced first-order recombination via well-defined PC84BM traps in organic bulk heterojunction solar cells. Adv. Funct. Mater. 21, 3083–3092. https://doi.org/10.1002/adfm.201100514.

Fru, J.N., Nombona, N., Diale, M., 2020a. Characterization of sequential physical vapor deposited methylammonium lead tri-iodide perovskite thin films. Vacuum 182, 109727. https://doi.org/10.1016/j.vacuum.2020.109727.

Fru, J.N., Nombona, N., Diale, M., 2020b. Synthesis and characterisation of methylammonium lead tri-bromide perovskites thin films by sequential physical vapor deposition. Phys. B Condens. Matter 578, 411884. https://doi.org/10.1016/j.physb.2019.411884.

Fru, J.N., Nombona, N., Diale, M., 2021. Characterization of thin MAPb(I1–xBrx)3 alloy halide perovskite films prepared by sequential physical vapor deposition. Front. Energy Res. 9, 1–17. https://doi.org/10.3389/fenrg.2021.667323.

He, Y., Liu, Z., McCall, K.M., Lin, W., Chung, D.Y., Wessels, B.W., Kanatzidis, M.G., 2019. Perovskite CsPbBr 3 single crystal detector for alpha-particle spectroscopy. Nucl. Instruments Methods Phys. Res. Sect. A Accel. Spectrometers, Detect. Assoc. Equip. 922, 217–221. https://doi.org/10.1016/j.nima.2019.01.008.

Jeon, N.J., Noh, J.H., Kim, Y.C., Yang, W.S., Ryu, S., Il Seok, S., 2014. Inorganic – Organic Hybrid Perovskite Solar Cells, pp. 1–7. https://doi.org/10.1038/NMAT4014.

Kim, H.S., Park, N.G., 2020. Importance of tailoring lattice strain in halide perovskite crystals. NPG Asia Mater. 12 https://doi.org/10.1038/s41427-020-00265-w.

Kim, J., Pearton, S.J., Fares, C., Yang, J., Ren, F., Kim, S., Polyakov, A.Y., 2019. Radiation damage effects in Ga2O3 materials and devices. J. Mater. Chem. C 7, 10–24. https://doi.org/10.1039/c8tc04193h.

Kim, T.S., Kim, H.J., Geum, D.M., Han, J.H., Kim, I.S., Hong, N., Ryu, G.H., Kang, J.H., Choi, W.J., Yu, K.J., 2021. Ultra-lightweight, flexible InGaP/GaAs tandem solar cells with a dual-function encapsulation layer. ACS Appl. Mater. Interfaces 13, 13248–13253. https://doi.org/10.1021/acsami.1c00006.

King, R.R., Fetzer, C.M., Law, D.C., Edmondson, K.M., Yoon, H., Kinsey, G.S., Krut, D.D., Ermer, J.H., Hebert, P., Cavicchi, B.T., Karam, N.H., 2006. Advanced III-V multijunction cells for space. In: Conf. Rec. 2006 IEEE 4th World Conf. Photovolt. Energy Conversion, WCPEC-4. 2, pp. 1757–1762. https://doi.org/10.1109/WCPEC.2006.279831.

Kundu, S., Kelly, T.L., 2020. In situ studies of the degradation mechanisms of perovskite solar cells. EcoMat 2, 1–22. https://doi.org/10.1002/eom2.12025.

Lang, F., Nickel, N.H., Bundesmann, J., Seidel, S., Denker, A., Albrecht, S., Brus, V.V., Rappich, J., Rech, B., Landi, G., Neitzert, H.C., 2016. Radiation hardness and self-healing of perovskite solar cells. Adv. Mater. 28, 8726–8731. https://doi.org/10.1002/adma.201603326.

Lang, F., Jo˘st, M., Bundesmann, J., Denker, A., Albrecht, S., Landi, G., Neitzert, H.-C., J¨org, R., Nickel, N.H., 2019. Efficient minority carrier detrapping mediating the radiation hardness of triple-cation perovskite solar cells under proton irradiation. Energy Environ. Sci. 12, 1634–1647. https://doi.org/10.1039/C9EE00077A.

Lang, F., Jo˘st, M., Frohna, K., K¨ohnen, E., Al-Ashouri, A., Bowman, A.R., Bertram, T., Morales-Vilches, A.B., Koushik, D., Tennyson, E.M., Galkowski, K., Landi, G., Creatore, M., Stannowski, B., Kaufmann, C.A., Bundesmann, J., Rappich, J., Rech, B., Denker, A., Albrecht, S., Neitzert, H.C., Nickel, N.H., Stranks, S.D., 2020. Proton radiation hardness of perovskite tandem photovoltaics. Joule 4, 1054–1069. https://doi.org/10.1016/j.joule.2020.03.006.

Li, J., Aierken, A., Liu, Y., Zhuang, Y., Yang, X., Mo, J.H., Fan, R.K., Chen, Q.Y., Zhang, S. Y., Huang, Y.M., Zhang, Q., 2021. A brief review of high efficiency III-V solar cells for space application. Front. Physiol. 8, 1–15. https://doi.org/10.3389/fphy.2020.631925.

Mahapatra, A., Parikh, N., Kumar, P., Kumar, M., Prochowicz, D., Kalam, A., Tavakoli, M. M., Yadav, P., 2020. Changes in the electrical characteristics of perovskite solar cells with aging time. Molecules 25, 1–10. https://doi.org/10.3390/molecules25102299.

Mayimele, M.A., Fru, J.N., Nyarige, J.S., Diale, M., 2022. Sequential physical vapor deposited methylammonium lead tri-iodide perovskites on FTO and ITO modified zinc oxide nanorods for perovskite solar cells. Phys. B Condens. Matter 625, 413462. https://doi.org/10.1016/j.physb.2021.413462.

Miyazawa, Y., Ikegami, M., Chen, H.W., Ohshima, T., Imaizumi, M., Hirose, K., Miyasaka, T., 2018. Tolerance of perovskite solar cell to high-energy particle irradiations in space environment. iScience 2, 148–155. https://doi.org/10.1016/j.isci.2018.03.020.

Mott, N.F., Davis, E.A., 1970. Conduction in non-crystalline systems V. Conductivity, optical absorption and photoconductivity in amorphous semiconductors. Philos. Mag. A 22, 903–922. https://doi.org/10.1080/14786437008221061.

Nassan, L., Abdalla, B., Omar, H., Sarheel, A., Alsomel, N., 2015. Locally manufactured films for neutron flux measurement in the MNSR type reactor. Ann. Nucl. Energy 83, 108–113. https://doi.org/10.1016/j.anucene.2015.04.014.

Nassan, L., Abdallah, B., Omar, H., Sarheel, A., Alsomel, N., Ghazi, N., 2016. Neutron energy spectrum adjustment using deposited metal films on Teflon in the miniature neutron source reactor. Appl. Radiat. Isot. 107, 239–246. https://doi.org/10.1016/j.apradiso.2015.10.036.

Nwankwo, V.U.J., Jibiri, N.N., Kio, M.T., 2020. The impact of space radiation environment on satellites operation in near-earth space. Satell. Mission. Technol. Geosci. 73–90. https://doi.org/10.5772/intechopen.90115.

Oryema, B., Jurua, E., Madiba, I.G., Ahmad, I., Aisida, S.O., Ezema, F.I., Maaza, M., 2022. Effects of 7 MeV proton irradiation on microstructural, morphological, optical, and electrical

properties of fluorine-doped tin oxide thin films. Surface. Interfac. 28, 101693 https://doi.org/10.1016/j.surfin.2021.101693.

Ramanujam, J., Singh, U.P., 2017. Copper indium gallium selenide based solar cells–a review. Energy Environ. Sci. 10, 1306–1319. https://doi.org/10.1039/C7EE00303J.

Redinger, A., Siebentritt, S., 2015. Loss mechanisms in kesterite solar cells, copp. Zinc tin sulfide-based thin-film. Sol. Cell. 627, 363–386. https://doi.org/10.1002/9781118437865.ch16.

Saidaminov, M.I., Abdelhady, A.L., Murali, B., Alarousu, E., Burlakov, V.M., Peng, W., Dursun, I., Wang, L., He, Y., MacUlan, G., Goriely, A., Wu, T., Mohammed, O.F., Bakr, O.M., 2015. High-quality bulk hybrid perovskite single crystals within minutes by inverse temperature crystallization. Nat. Commun. 6, 1–6. https://doi.org/10.1038/ncomms8586.

Schock, H.W., Noufi, R., 2000. CIGS-based solar cells for the next millennium. Prog. Photovoltaics Res. Appl. 8, 151–160. https://doi.org/10.1002/(SICI)1099-159X(200001/02)8:1<151::AID-PIP302>3.0.CO;2-Q.

Shi, D., Adinolfi, V., Comin, R., Yuan, M., Alarousu, E., Buin, A., Chen, Y., Hoogland, S., Rothenberger, A., Katsiev, K., Losovyj, Y., Zhang, X., Dowben, P.A., Mohammed, O. F., Sargent, E.H., Bakr, O.M., 2015. Low trap-state density and long carrier diffusion in organolead trihalide perovskite single crystals. Science 347, 519–522. https://doi.org/10.1126/science.aaa2725.

Shkir, M., Khan, A., El-Toni, A.M., Aldalbahi, A., Yahia, I.S., AlFaify, S., 2019. Structural, morphological, opto-nonlinear-limiting studies on Dy: PbI_2/FTO thin films derived facilely by spin coating technique for optoelectronic technology. J. Phys. Chem. Solid. 130, 189–196. https://doi.org/10.1016/j.jpcs.2019.02.030.

Siddiqui, A., Usman, M., 2021. Reliability of perc solar cells under alpha irradiation: a simulation-based study for space applications. ECS J. Solid State Sci. Technol. 10, 015003 https://doi.org/10.1149/2162-8777/abdadf.

Song, Z., Li, C., Chen, C., McNatt, J., Yoon, W., Scheiman, D., Jenkins, P.P., Ellingson, R. J., Heben, M.J., Yan, Y., 2020. High remaining factors in the photovoltaic performance of perovskite solar cells after high-fluence electron beam irradiations. J. Phys. Chem. C 124, 1330–1336. https://doi.org/10.1021/acs.jpcc.9b11483.

Tan, R., Dryzhakov, B., Charest, J., Hu, B., Ahmadi, M., Lukosi, E., 2021. Improved radiation sensing with methylammonium lead tribromide perovskite semiconductors. Nucl. Instruments Methods Phys. Res. Sect. A Accel. Spectrometers, Detect. Assoc. Equip. 986, 164710 https://doi.org/10.1016/j.nima.2020.164710.

Williamson, G.K., Hall, W.H., 1953. X-ray line broadening from filed aluminium and wolframL'elargissement des raies de rayons x obtenues des limailles d'aluminium et de tungsten Die verbreiterung der roentgeninterferenzlinien von aluminium- und wolframspaenen. Acta Metall. 1, 22–31. https://doi.org/10.1016/0001-6160(53)90006-6.

Xu, J., Guo, M., Lu, M., He, H., Yang, G., Xu, J., 2018. Effect of alpha-particle irradiation on InGaP/GaAs/Ge triple-junction solar cells. Materials 11, 1–9. https://doi.org/10.3390/ma11060944.

Xu, Q., Zhang, H., Nie, J., Shao, W., Wang, X., Zhang, B., Ouyang, X., 2021. Effect of methylammonium lead tribromide perovskite based-photoconductor under gamma photons radiation. Radiat. Phys. Chem. 181, 109337 https://doi.org/10.1016/j.radphyschem.2020.109337.

Yang, S., Xu, Z., Xue, S., Kandlakunta, P., Cao, L., Huang, J., 2019. Organohalide lead perovskites: more stable than Glass under gamma-ray radiation. Adv. Mater. 31, 1805547 https://doi.org/10.1002/adma.201805547.

Zhang, L., Hu, T., Li, J., Zhang, L., Li, H., Lu, Z., Wang, G., 2020. All-inorganic perovskite solar cells with both high open-circuit voltage and stability. Front. Mater. 6, 330.
https://doi.org/10.3389/fmats.2019.00330.